CHEMISTRY OF MATERIALS

ARTICLE

pubs.acs.org/cm

# Controlling Zeolitic Imidazolate Framework Nano- and Microcrystal Formation: Insight into Crystal Growth by Time-Resolved In Situ Static Light Scattering

Janosch Cravillon,[†] Roman Nayuk,[‡] Sergej Springer,[†] Armin Feldhoff,[§] Klaus Huber,[*,‡] and Michael Wiebcke[*,†]

[†]Institut für Anorganische Chemie, Leibniz Universität Hannover, Callinstr. 9, 30167 Hannover, Germany

[‡]Department Chemie, Universität Paderborn, Warburger Str. 100, 33098 Paderborn, Germany

[§]Institut für Physikalische Chemie und Elektrochemie, Leibniz Universität Hannover, Callinstr. 3A, 30167 Hannover, Germany

Supporting Information

**ABSTRACT:** We report on a simple and straightforward method that enables the rapid room-temperature production of nanocrystals (finely tuned in size between ~10 and 65 nm) and microcrystals (~1 $\mu$m) of the prototypical microporous zeolitic imidazolate framework (ZIF) material ZIF-8. Control of crystal size is achieved in a novel approach by employing an excess of the bridging bidentate ligand and various simple auxiliary monodentate ligands with different chemical functionalities (carboxylate, *N*-heterocycle, alkylamine). The function of the monodentate ligands can be understood as a modulation of complex formation *and* deprotonation equilibria during crystal nucleation and growth. Using time-resolved static light scattering, the functioning of modulating ligands is monitored for the first time by in situ experiments, which offered significant insight into the crystal growth processes. Formation of nanocrystals is characterized by continuous, comparatively slow nucleation and fast crystal growth occurring on a time scale of seconds. Although nucleation and growth are not separated from each other, a significant narrowing of the particle size distribution during early stages results in rather monodisperse nanocrystals, before broadening of the particle size distribution occurs, as observed by complementary ex situ electron microscopy studies. Microcrystal growth is dominated by a particle−monomer addition mechanism, but indications for the operation of a coalescence process during early stages of growth have been also obtained. During later stages of microcrystal growth crystals change their shape from cubes to rhombic dodecahedra. The prepared phase-pure ZIF-8 nanoscale materials exhibit good thermal stability in air and large surface areas, which are comparable to those of large macrocrystals. Nanocrystal powders exhibit dual micro- and mesoporosity.

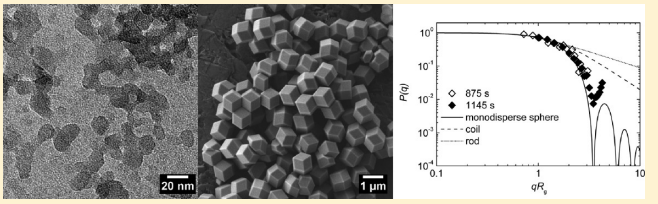


**KEYWORDS:** metal−organic framework, zeolitic imidazolate framework, nanomaterials, modulated synthesis, crystal growth, in situ static light scattering

## INTRODUCTION

Zeolitic imidazolate framework (ZIF) materials[1] constitute a new distinctive, rapidly developing subclass of crystalline porous coordination polymers (PCPs) or metal−organic frameworks (MOFs).[2] For example, bulk ZIF materials[3] and supported ZIF membranes and films[4] have shown promising properties in the fields of $CO_2$ capture and storage, separation of light gases, sensing of vapors, and heterogeneous catalysis. The three-periodic tetrahedral framework structures of ZIFs are constructed from bivalent metal cations and bridging substituted imidazolate anions and frequently possess a zeolite topology.[1,5] Numerous ZIFs combine the attractive features of MOFs (diversity of framework structures and pore systems, large surface areas, post-synthetically modifiable organic bridging ligands) with high thermal and chemical stability.[6] It is this combination of properties which makes ZIFs very promising candidate materials for many technological applications. On the other hand, properties and performance of porous materials rely much on their supply as nano- and microcrystals of well-defined size and shape, as is well-known for zeolites.[7] Development of size- and shape-controlled syntheses, in turn, benefits considerably from a detailed understanding of the physicochemical fundamentals of the crystallization processes.[8]

These important issues have only scarcely been addressed in the field of porous MOFs. A limited number of carboxylate-based nanoscale MOFs have been prepared, for example, by reverse microemulsion methods and microwave- or ultrasound-assisted syntheses.[9,10] A very attractive approach to controlling crystal size and shape that has been recently introduced is the coordination modulation method which employs an auxiliary monodentate ligand that acts in competition to the multidentate bridging ligand at surface-exposed metal centers of the forming

**Received:** December 15, 2010
**Revised:** February 24, 2011
**Published:** March 18, 2011

crystals.[11,12] Such modulating ligands are usually monocarboxylates, having the same chemical functionality as the bridging polycarboxylate ligands. The power of this method has been very recently demonstrated by Kitagawa and co-workers[12b] who were able to prepare $[Cu_3(btc)_2]$ crystals (HKUST-1, btc = benzene-1,3,5-tricarboxylate) in the whole range from the small nanoscale (~20 nm) to the microscale (~2 $\mu$m). First insight into the mechanisms of carboxylate-based MOF crystallization has been obtained by a number of recent in situ investigations employing static light scattering,[11a,13] surface plasmon resonance spectroscopy,[14] atomic force microscopy,[15] and energy-dispersive X-ray diffraction.[16] Furthermore, the growth of nanorods of a carboxylate-based MOF by oriented attachment has been demonstrated in a remarkable ex situ electron microcopy study.[12a]

Progress is still more limited for ZIFs. We have recently reported in a preliminary communication on a simple and rapid room-temperature solution-based synthesis of ~45 nm-sized ZIF-8 nanocrystals with a rhombic dodecahedral shape and a narrow size distribution.[17] Such ZIF-8 nanocrystals have meanwhile been used to fabricate porous composite nanofibers by electrospinning,[18] supported membranes with random[19] and preferred crystal orientation for gas separation,[20] thin films with dual micro- and mesoporosity for selective adsorption and sensing of vapors,[21] and capillary coatings for the chromatographic separation of alkanes,[22] indicating the wide range of potential applications of nanoscale ZIF materials. Later, Thallapally and co-workers[23] have also prepared ~50 nm-sized ZIF-8 nanocrystals in a similar approach but with the addition of an organic polymer, claiming that the nanocrystals have a hexagonal shape. In addition, Li and co-workers[24] have recently reported on spherical ZIF-7 nanocrystals as well as ZIF-7 nano- and microrods. All these successful syntheses of nano- and microscale ZIF materials had to be developed empirically by exploratory synthetic work, since a detailed understanding of the crystallization processes is missing.

In order to gain a better understanding of the mechanisms of ZIF crystallization and thereby put the synthesis of ZIF materials on a more rational basis, we have combined systematic synthetic work with time-resolved experiments, namely, in situ static light scattering (SLS) and ex situ scanning electron microscopy (SEM). Herein, we demonstrate for the first time that various simple modulating monodentate ligands with different functionalities (sodium formate, 1-methylimidazole, *n*-butylamine) can be used in rapid room-temperature syntheses to tune the size of ZIF-8 crystals between ~10 nm and 1 $\mu$m. Along with this, significant insight is presented into ZIF-8 crystallization processes. We further demonstrate that the prepared nanoscale ZIF-8 materials are easily activated and exhibit good thermal stability in air as well as large surface areas.

## EXPERIMENTAL SECTION

**Materials.** Commercially available chemicals were used without further purification (see Supporting Information). All syntheses were performed at ambient conditions.

**Synthesis of ZIF-8 Nanocrystals in the Absence of a Modulating Ligand.** Typically, 734.4 mg (2.469 mmol) of $Zn(NO_3)_2 \cdot 6H_2O$ and 810.6 mg (9.874 mmol) of 2-methylimidazole (Hmim) are each dissolved in 50 mL of MeOH. The latter clear solution is poured into the former clear solution under stirring with a magnetic bar. Stirring is stopped after combining the component solutions. After 24 h, the solid is separated from the milky colloidal dispersion by centrifugation. Washing with fresh MeOH and centrifugation is repeated three times. The product is dried at room-temperature under reduced pressure.

**Synthesis of ZIF-8 Microcrystals with Sodium Formate or 1-Methylimidazole As a Modulating Ligand.** Typically, 734.4 mg (2.469 mmol) of $Zn(NO_3)_2 \cdot 6H_2O$ is dissolved in 50 mL of MeOH. A second solution is prepared by dissolving 810.6 mg (9.874 mmol) of Hmim and 810.6 mg (9.874 mmol) of 1-methylimidazole in 50 mL of MeOH. The latter clear solution is poured into the former clear solution under stirring with a magnetic bar. Stirring is stopped after combining the component solutions. After 24 h, the precipitate is recovered by filtration, washing with MeOH, and drying under reduced pressure. Syntheses in the presence of sodium formate is made similarly (see Supporting Information).

**Synthesis of ZIF-8 Nanocrystals with *n*-Butylamine as a Modulating Ligand.** Typically, 734.4 mg (2.469 mmol) of $Zn(NO_3)_2 \cdot 6H_2O$ is dissolved in 50 mL of MeOH. A second solution is prepared by dissolving 810.6 mg (9.874 mmol) of Hmim and 0.975 mL (9.874 mmol) of *n*-butylamine in 50 mL of MeOH. The latter clear solution is poured into the former clear solution under stirring with a magnetic bar. Stirring is stopped after combining the component solutions. After 24 h, the gel-like solid is recovered by centrifugation. Washing with fresh MeOH and centrifugation is repeated three times. The product is dried at room-temperature under reduced pressure. Syntheses with variation of the molar ratios were made similarly.

**Methods of Characterization.** Powder X-ray diffraction (XRD) at room temperature was performed in transmission mode on a STOE Stadi-P diffractometer using monochromatized Cu $K\alpha_1$ radiation of wavelength $\lambda$ = 1.54059 Å. The instrumental peak broadening needed for Scherrer analysis was determined using a silicon reference standard (NIST 640c). For intensity data recording at variable temperatures in Debye−Scherrer geometry, the same diffractometer was equipped with a STOE high-temperature oven. Samples were filled into thin-walled silica glass capillaries (diameter 0.5 mm) which were left unsealed.

Small-angle X-ray scattering (SAXS) measurements were performed in transmission mode on a RIGAKU system consisting of a microfocus X-ray tube with Cu target and mirror optics ($\lambda$ = 1.541 Å), a three-pinhole collimating system, and a 2D gas-filled multiwire detector. Colloidal solutions were filled into thin-walled glass capillaries (diameter 1.5 mm), while powder samples were kept between thin Kapton foils. SANS Analysis software[25] provided by the NIST Center for Neutron Research was used for model fitting of SAXS curves in reciprocal space. Indirect Fourier transformation was applied to obtain pair distance distribution functions (PDDFs)[26] in direct space from the SAXS data by using the progam GNOM.[27]

Thermogravimetry (TG) and difference thermal analysis (DTA) measurements were performed simultaneously on a NETZSCH 429 Thermoanalyzer. Samples were filled into alumina crucibles and heated in a flow of air with a ramp of 5 °C·min$^{-1}$ from room temperature up to 1000 °C.

Nitrogen physisorption isotherms were measured at −196 °C on a QUANTACHROME Autosorb1-MP volumetric instrument. Samples were outgassed in vacuum at room temperature for at least 24 h before the sorption measurements. Surface areas were estimated by applying the Brunauer−Emmett−Teller (BET) equation. The Barrett−Joyner−Halenda (BJH) method was applied to determine mesopore size distributions.

Fourier-transform infrared (FT-IR) spectra were recorded on a BRUKER Tensor 27 spectrometer using the attenuated total reflection (ATR) technique.

Scanning electron micrographs (SEM) were taken in secondary electron contrast at an acceleration voltage of 2 keV using a JEOL JSM-6700F field-emission instrument. Samples were dispersed on a carbon sample holder. Transmission electron microscopy (TEM) micrographs

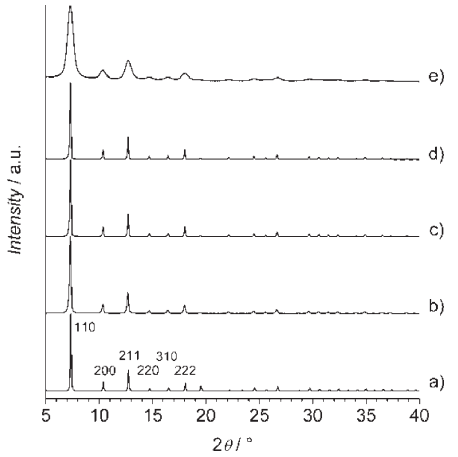


**Figure 1.** XRD patterns (a) simulated from crystal structure, (b) of 65 nm-sized nanocrystals prepared in the absence of a modulating ligand, (c) of microcrystals prepared in the presence of sodium formate, (d) of microcrystals prepared in the presence of 1-methylimidazole, and (e) of 18 nm-sized nanocrystals prepared in the presence of *n*-butylamine.

were taken using a JEOL JEM-2100F-UHR field-emission instrument at an acceleration voltage of 200 kV. The same instrument was used for taking selected area electron diffraction (SAED) patterns. Samples were collected with a syringe from the colloidal solutions and dispersed on a copper-supported carbon film.

**Time-Resolved in Situ Static Light Scattering (SLS).** SLS measurements were performed at 25 °C with a home-built multi-angle goniometer described by Becker and Schmidt.[28] Cylindrical silica glass cuvettes with a diameter of 25 mm served as scattering cells. The goniometer was equipped with a He-Ne laser operating at a wavelength of 632.8 nm. It enabled simultaneous recording of the scattering intensity at 2 times 19 scattering angles arranged in pairs symmetrically on both sides of the beam in an angular regime of $25.84° \leq \theta \leq 143.13°$. Recording of an angular dependent curve was completed after 2 ms. 1000 successive recordings were added to form one measurement requiring 2 s in total. The time interval between the start of the successive measurements was 10 s. The component solutions (see syntheses) were cleaned by passing the solutions through 0.20 $\mu$m filters to remove dust particles and to combine them into the scattering cell. Addition of the second component solution determined the starting point ($t = 0$) of the experiment. Scattering curves were processed as the Rayleigh ratio $\Delta R_\theta$ at variable scattering angle $\theta$.[29] The scattering curves could be approximated by means of a Guinier plot,[30] which enabled the extraction from each scattering curve the accumulated weight-averaged molar mass, $M_W$, and the square root of the *z*-averaged squared radius of gyration, $R_g$ (details are provided in the Supporting Information).

## RESULTS AND DISCUSSION

Our approach to the size-controlled synthesis of nano- and microscale ZIF materials is an extension of the method we have recently developed for the production of ~45 nm-sized ZIF-8 nanocrystals. It employs an excess of the bridging 2-methylimidazole (Hmim) ligand with respect to the Zn(II) source, $Zn(NO_3)_2 \cdot 6H_2O$, in methanolic solutions.[17] This simple method works already well at room temperature without the need of any activation, for example, by conventional or microwave heating. We have now added to such ZIF-8 synthesis solutions various monodentate ligands with different chemical functionalities (carboxylate, *N*-heterocycle, alkylamine). This is in contrast to related previous work, where the coordination modulation

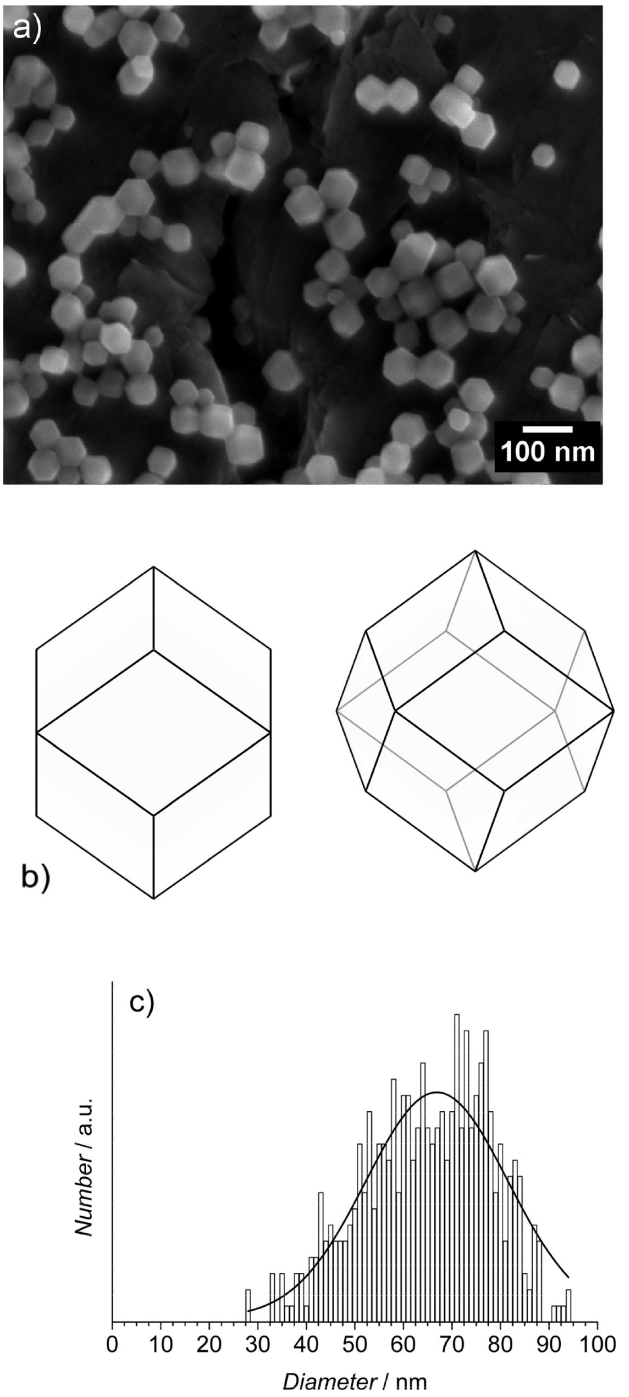


**Figure 2.** (a) SEM image of 65 nm-sized nanocrystals prepared in the absence of a modulating ligand, (b) drawings of a rhombic dodecahedron in two orientations, and (c) size distribution of 65 nm-sized nanocrystals (the line represents a Gaussian fit).

method has been employed in the synthesis of carboxylate-based MOFs with modulating ligands with only the same carboxylate functionality as the bridging ligands.[11,12] We note that modulating ligands do not only act as competitive ligands at the metal centers but also as bases on the deprotonation of the bridging ligands. Thus, they may affect crystal nucleation and growth via both coordination and deprotonation equilibria. This combined effect has not been investigated and utilized before.

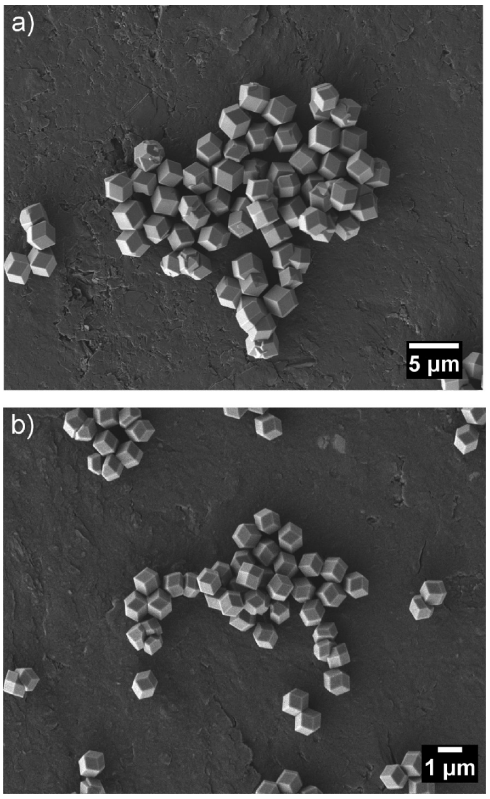


**Figure 3.** SEM images of (a) microcrystals prepared in the presence of sodium formate and (b) microcrystals prepared in the presence of 1-methylimidazole.

**Synthesis of the Nano- and Microcrystals.** We first investigated synthesis solutions with the total molar ratio Zn/Hmim/L/MeOH = 1:4:*x*:1000 (L = modulating ligand: sodium formate,1-methylimidazole, *n*-butylamine). The products were isolated as described in the Experimental Section after 24 h of reaction at room temperature. The synthesis without addition of a modulating ligand ($x = 0$) yields pure-phase ZIF-8 nanocrystals (compare the XRD patterns in Figure 1a,b) with an average particle size of 64 nm, as estimated from the broadening of the Bragg reflections by applying Scherrer's equation. SEM images (Figure 2a) reveal that the well-defined nanocrystals have a rhombic dodecahedral shape (see Figure 2b for comparison) with 12 exposed {110} faces. This is a special crystal form of the crystallographic point group $\bar{4}3m$ (in line with the cubic space group $I\bar{4}3m$ of crystalline ZIF-8).[6] We note that rhombic dodecahedra, when viewed directly on a {110} face, appear with a hexagonal cross-section (see drawing on the left-hand side of Figure 2b). Thus, care has to be taken not to mix up rhombic dodecahedral nanocrystals on SEM or TEM images with a hexagonal shape, which may have happened in recent work[23] (further comments on this point are given in the Supporting Information). A statistical evaluation of 500 particles results in an average size of 65 ± 13 nm (see size distribution in Figure 2c). The nanocrystals are redispersible in MeOH, yielding dispersions of nearly nonaggregated particles from which sedimentation occurs only very slowly. SAXS analysis results in an average size for the redispersed particles of 88 nm. A SAXS pattern taken from a dispersion along with a fitted curve obtained with a model of polydisperse spherical particles is provided in Figure S2 of the Supporting Information.

In the presence of formate or 1-methylimidazole as a modulating ligand at $x = 4$, pure-phase ZIF-8 microcrystals are obtained (see XRD patterns in Figure 1c,d). SEM images (Figure 3a,b) reveal a rhombic dodecahedral shape and a remarkable narrow size distribution. There is no significant difference between the products despite the quite different nature of the modulating ligands (anionic carboxylate vs neutral N-heterocyclic molecule). It should be noted that the narrow size distribution is only obtained when the synthesis solutions are not stirred. Stirring results in very broad size distributions, which may be due to secondary nucleation caused by turbulences.[31]

When *n*-butylamine is added as the modulating ligand at $x = 4$, nearly instantaneous formation of a solid is observed upon combining the component solutions, and pure-phase ZIF-8 nanocrystals are recovered after 24 h (see XRD pattern in Figure 1e). An average size of 18 nm is estimated from the broadening of the Bragg reflections. TEM images (Figure 4a) show roughly spherical particles being <20 nm in size, including some isolated particles and particles with sharp edges. It should be noted that the small ZIF nanocrystals are very sensitive to the high energy of the electron beam of a TEM.[17] SAED patterns (Figure 4b) confirm that the particles are crystalline ZIF-8. The nanocrystals can be redispersed in MeOH. According to a SAXS analysis, the redispersed particles indicate the primary 18 nm-sized nanoparticles. Yet, they now form small secondary aggregates with a maximum size of ~88 nm and an average radius of gyration of $R_g$ = 27 nm. A SAXS pattern along with the corresponding pair distance distribution function (PDDF) is provided in Figure S3 of the Supporting Information. The dispersions remain optically clear for a few hours, before a fine precipitate begins to form.

Then, we varied the molar ratios of the components in the system Zn/Hmim/*n*-butylamine/MeOH. Table 1 lists the compositions of the studied synthesis solutions and the average sizes of the obtained particles. XRD demonstrates that all products are pure-phase ZIF-8 (see Figure S5 of the Supporting Information). Particle sizes were determined from the powder samples by XRD (Scherrer's equation) and SAXS (PDDF), thus providing information on both the size of the crystalline domains (XRD) and the primary particles (SAXS). Compared to TEM, which is usually used to analyze primary particle size, SAXS has two advantages: (i) SAXS probes a much larger sample volume, which is therefore representative for the whole sample, and (ii) SAXS is nondestructive to ZIF nanocrystals. The PDDF, obtained by indirect Fourier transformation of a SAXS curve, is a representation of the intraparticle distance distribution, and in the case of homogeneous monodisperse spherical particles exhibits a maximum close to the radius of the spheres.[26] This behavior is preserved for powders consisting of spherical particles, where a maximum or shoulder is still observed at about the distance that corresponds to the radius of the primary particles.[32] Representative SAXS patterns along with the corresponding PDDF curves are displayed in Figure 5 (the remaining SAXS and PDDF data are provided in Figure S4 of the Supporting Information). As can be seen from Table 1, the size values determined by XRD and SAXS are in good agreement for the products, confirming that the primary particles are crystalline ZIF-8. In addition, it can be also seen from Table 1 that by varying the compositions of the synthesis solutions, the nanocrystal size can be tuned between 9 and 65 nm. It should be noted that the volume of the smallest nanocrystals (diameter 9 nm) corresponds to only 78 unit cells of ZIF-8 (cubic cell constant $a = 1.7012$ nm).[6b]

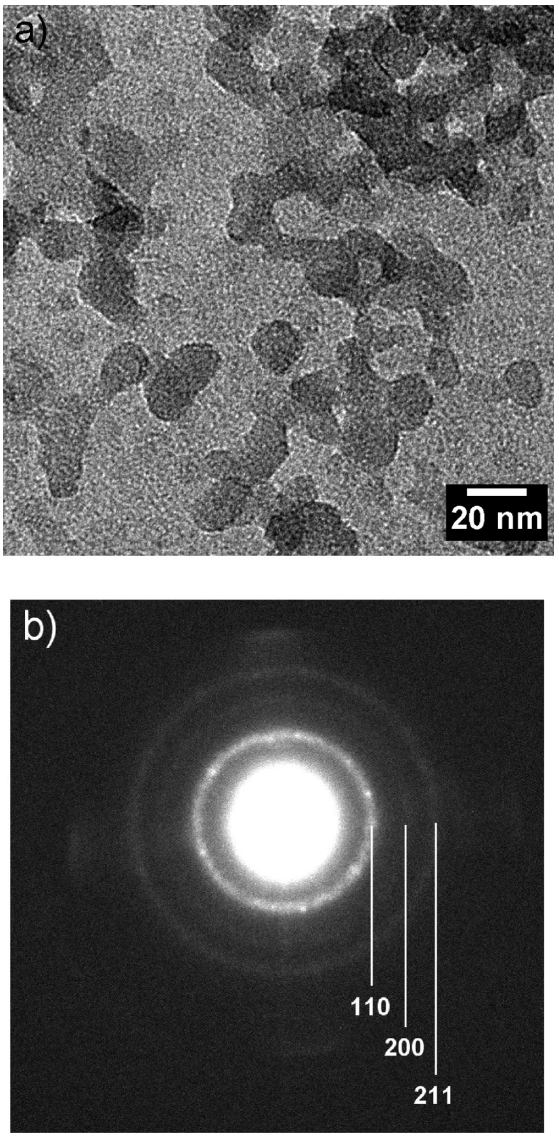


**Figure 4.** (a) TEM image and (b) SAED pattern of 18 nm-size nanocrystals prepared in the presence of *n*-butylamine.

By employing an excess of the bridging bidentate ligand together with different modulating ligands we have not only been able to achieve size control from the smallest nanoscale (~10 nm) to the microscale but, in addition, could gain new insight into the functioning of modulating ligands during MOF crystallization. In previous work,[12] only the effect of modulators on the coordination equilibria during nucleation and growth had been considered. In order to rationalize the outcome of our present syntheses we have to take deprotonation equilibria into consideration in addition to coordination equilibria. Scheme 1 summarizes in a simplified manner the basic reactions of ZIF-8 formation that have to be considered, namely, (i) complex formation, (ii) deprotonation, and (iii) ligand exchange. Due to the labile nature of Zn(II) complexes all equilibria are likely to be attained fast. Unfortunately, a complete set of the relevant complex formation constants is not available in the literature. We can, however, base a first qualitative discussion on the deprotonation constants of the conjugate acids of the ligands, which are provided in Scheme 1 in the form of p$K_a$ values (for aqueous

**Table 1. Compositions of Synthesis Solutions in the System Zn/Hmim/*n*-Butylamine/Methanol and Average Diameters of ZIF-8 Nanocrystals As Determined by XRD and SAXS**

| | composition | nanocrystal diameter | |
|---|---|---|---|
| | Zn/Hmim/*n*-BuNH$_2$/MeOH | $d_{XRD}$, nm | $d_{SAXS}$, nm |
| (1) | 1:4:4:1000 | 18 | 17 |
| (2) | 1:2:4:1000 | 45 | 39 |
| (3) | 1:4:2:1000 | 10 | 9 |
| (4) | 1:4:4:5000 | 24 | 20 |
| (5) | 1:2:4:5000 | 55 | 40 |
| (6) | 1:4:2:5000 | 9 | 9 |
| (7) | 1:4:4:500 | 16 | 16 |
| (8) | 1:2:4:500 | 43 | 42 |
| (9) | 1:4:2:500 | 10 | 8 |

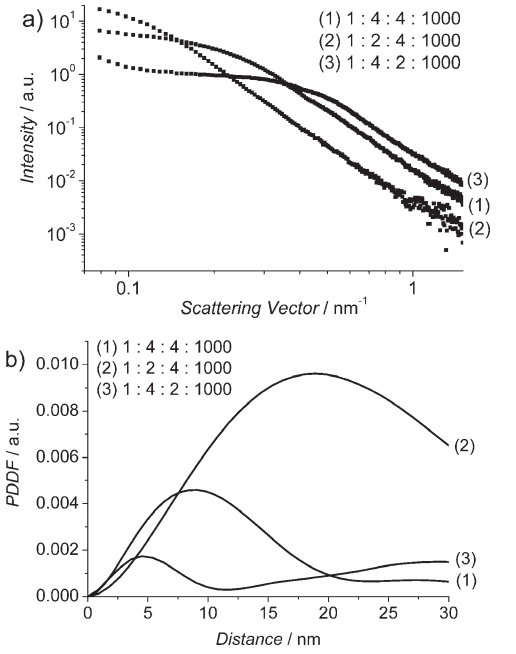


**Figure 5.** (a) Representative SAXS patterns and (b) inner parts of the corresponding PDDF curves of nanocrystals prepared in the presence of *n*-butylamine. Compositions of the synthesis solutions are indicated.

media, as an approximation for methanolic solutions). The list of p$K_a$ values includes an estimate for the deprotonation constant of Hmim being bound to a Zn(II) cation, as taken from the work by Kimura et al.[33] Hereby, the following explanations can be given for the syntheses with constant total molar ratios Zn/Hmim/L/MeOH = 1:4:4:1000. An excess of Hmim in reaction (i) yields, at the beginning of ZIF-8 formation, a high concentration of $[Zn(Hmim)_mL_n]$ species with $m > n$, which via deprotonation (ii) and ligand exchange (iii) results in a high nucleation rate and consequently in a small size of the final crystals (~65 nm in our case). Only the more basic modulating ligands with p$K_a$ > 10.3 can deprotonate the $[Zn(Hmim)_mL_n]$ species and thereby accelerate ligand exchange reactions, resulting in an even higher nucleation rate and consequently in a smaller final crystal size (~18 nm in our case). On the other hand, the less basic modulating ligands with p$K_a$ < 10.3 cannot effectively deprotonate $[Zn(Hmim)_mL_n]$ species but compete in reaction (i) with


dx.doi.org/10.1021/cm103571y |*Chem. Mater.* 2011, 23, 2130–2141

**Scheme 1. Basic Reactions of ZIF-8 Formation (Top) and $pK_a$ Values for the Conjugate Acids of Relevant Ligands (Bottom)**[a]

(i) $Zn + m\ Hmim + n\ L \rightleftharpoons [Zn(Hmim)_mL_n]$

(ii) $[Zn(Hmim)_mL_n] + L' \rightleftharpoons [Zn(Hmim)_{m-1}(mim)L_n] + HL'$

(iii) $[Zn(Hmim)_mL_n] + [Zn(Hmim)_{m-1}(mim)L_n]$

$+L \uparrow\downarrow -L$

$[(Hmim)_mL_{n-1}Zn(\mu\text{-}mim)Zn(Hmim)_{m-1}L_n]$

$\uparrow\downarrow$

oligomers, particles, crystals

$\uparrow\downarrow$

$[Zn(mim)_2]$

| ligand | $pK_a$ |
|---|---|
| HCOOH | 3.8 |
| $H_2mim^+$ | 7.0 |
| 1-Methylimidazolium | 7.2 |
| $[Zn(Hmim)]^{2+}$ | 10.3 |
| $n\text{-}BuNH_3^+$ | 10.7 |
| Hmim | 14.2 |

[a] Charges of species are omitted in the reaction equations. L denotes all ligands that may be present: Auxiliary modulating ligands as well as $NO_3^-$, $H_2O$, and MeOH.

Hmim, resulting in a low concentration of $[Zn(Hmim)_mL_n]$ species with $m > n$, in a low nucleation rate and consequently in a large final crystal size (~1 $\mu$m in our case). The modulating ligands also affect crystal growth (see below), but their influence on nucleation appears to be more important. For a more detailed understanding, knowledge of the complex formation and deprotonation constants in methanol would be required. The results of the syntheses in the Zn/Hmim/*n*-butylamine/MeOH system at variable molar ratios (Table 1) suggest that, for targeting particular small nanocrystals, an excess of the bridging ligand is the dominating factor (e.g., compare compositions 1, 2, and 3 in Table 1). Increasing the content of the *n*-butylamine base obviously does not lead to a smaller particle size, because then its function as a competitive ligand comes into play (e.g., compare compositions 1 and 3 in Table 1).

**Time-Resolved in Situ SLS and ex Situ SEM Investigations of Nanocrystal Formation.** Particle formation could be successfully monitored by SLS with synthesis solutions of composition Zn/Hmim/MeOH = 1:4:1000, yielding 65 nm-sized nanocrystals. From each scattering pattern the accumulated weight-averaged molar mass, $M_W$, and the square root of the *z*-averaged squared radius of gyration, $R_g$, were extracted for the growing particles. The evolution with time of these parameters is displayed in Figure 6a. Nanoparticles with a radius of gyration of $R_g \approx 20$ nm (corresponding to $R_{sphere} = 26$ nm) become detectable for the first time after 130 s. The size of these particles corresponds to approximately 3/4 of the size of the final nanocrystals recovered after 24 h from the synthesis solution, and the particles are likely to be crystalline. During the following 670 s the total particle mass increases continuously, while the average particle size remains essentially constant. This apparent

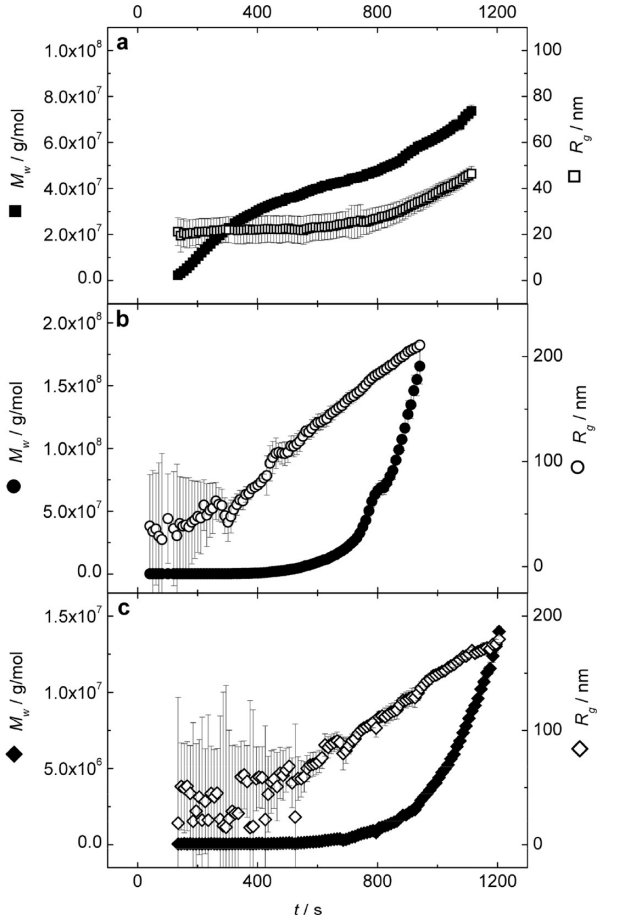


**Figure 6.** Weight-averaged particle mass, $M_W$, and radius of gyration, $R_g$, as they evolve with time for (a) the formation of 65 nm-sized nanocrystals in the absence of a modulating ligand, (b) the formation of microcrystals in the presence of sodium formate, and (c) the formation of microcrystals in the presence of 1-methylimidazole. Error bars are shown for $R_g$ values.

inconsistency can be interpreted as follows. Single particles grow very fast compared to the time resolution of our experiment, and the individual growth becomes slow when a size close to $R_g$ = 20 nm is attained. The increase in the averaged particle mass $M_w$ (of a bimodal system composed of small building units and particles) is predominantly due to a continuous and comparatively slow nucleation, which increases the number of particles with time. The averaged squared size $R_g^2$ and the averaged mass values $M_W$ are based on different averaging procedures. Whereas $R_g^2$ corresponds to the third moment, $M_W$ is the second moment of the particle mass distribution. Thus, the average square of the size weights larger particles stronger than the average mass does. As a consequence, $R_g^2$ of an ever increasing ensemble of particles with similar size values approaches its final average value much earlier than $M_W$ does.

After approximately 800 s the particle size and mass increases. This is due to a loose agglomeration of the primary nanoparticles which essentially keep their size, as evidenced by SEM investigations (see below). As can be seen from Figure 7a, this agglomeration stage is indicated by a steep upturn in the $\log(R_g)$ vs $\log(M_W)$ plot. The analysis during the agglomeration stage is impaired by an increasing turbidity of the dispersions causing multiple scattering. This results in mass values which increasingly


dx.doi.org/10.1021/cm103571y |*Chem. Mater.* 2011, 23, 2130–2141

depart toward lower values, which prevents further quantitative interpretation of the upturn. Note that, after the beginning of the agglomeration stage, SLS can give no information anymore of whether nucleation still further continues or stops after some time.

For complementary SEM investigations, small amounts of liquid were taken from the synthesis solutions after 240 s (before the agglomeration stage) and after 1 h (during the agglomeration stage). After 240 s, spherical particles with an average size of 42 ± 11 nm and some amorphous material adhering to the particles are observed (see SEM image in Figure 8a). The particle size distribution (Figure 8c) is comparatively broad. This supports the above interpretation of the SLS data that slow, persistent nucleation and fast crystal growth take place in the early stages of nanoparticle formation. After 1 h, the nanoparticles still have nearly the same size, 38 ± 4 nm (see SEM image in Figure 8b).

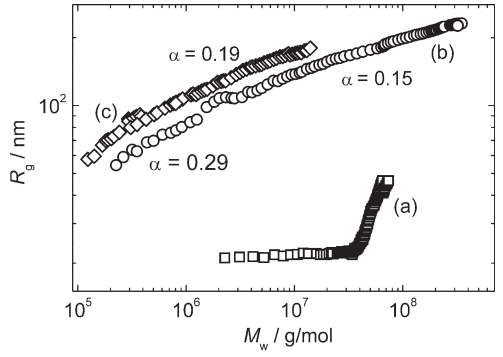


**Figure 7.** log($R_g$) vs log($M_W$) plot for (a) the formation of 65 nm-sized nanocrystals in the absence of a modulating ligand, (b) the formation of microcrystals in the presence of sodium formate, and (c) the formation of microcrystals in the presence of 1-methylimidazole.

This clearly proves that the steep increase in size and mass at 800 s observed by SLS is an agglomeration of primary nanocrystals with $R_g \approx 20$ nm. Importantly, the size distribution (Figure 8d) has become very narrow after 1 h. The nanoparticles with an age of 1 h are crystalline ZIF-8 and have a rhombic dodecahedral shape (see SEM image in Figure 8b and the detailed XRD and TEM characterization of similar nanocrystals presented elsewhere)[17] as the final 65 nm-sized nanocrystals recovered after 24 h (see SEM image in Figure 2a). Note that the final nanocrystals (size 65 ± 13 nm) have a considerably broader size distribution (Figure 2c) as the nanocrystals with an age of 1 h.

Narrowing ("focusing") of size distribution was first experimentally observed for semiconductor nanoparticles[34] and is reported here for the first time for a MOF. In this case, however, the narrowing of the size distribution of the primary nanocrystals at intermediate stages (after ~1 h) and, in particular, the very narrow size distribution at the size focusing point are rather surprising findings considering the observation by SLS that slow nucleation occurs together with fast growth at least for the first 800 s of the crystallization process. This means that nucleation and growth are not well separated from each other. Separation of both steps is usually believed to be necessary to obtain particles of low polydispersity (LaMer mechanism of burst nucleation and subsequent growth).[8,34] The "focusing" may be explained by the termination of the fast particle growth at a size of $R_g \approx 20$ nm, due to colloidal stabilization of these intermediate particles by surface-coordinated neutral, nondeprotonated Hmim ligands that are present in excess and a corresponding build-up of positive surface charges and favorable interactions with the polar solvent. The effect of positive surface charges is supported experimentally by a zeta potential of $\xi = +55$ mV for ZIF-8 nanocrystals redispersed in MeOH.[17] After supersaturation has sufficiently decreased and nucleation ceased, all nanoparticles

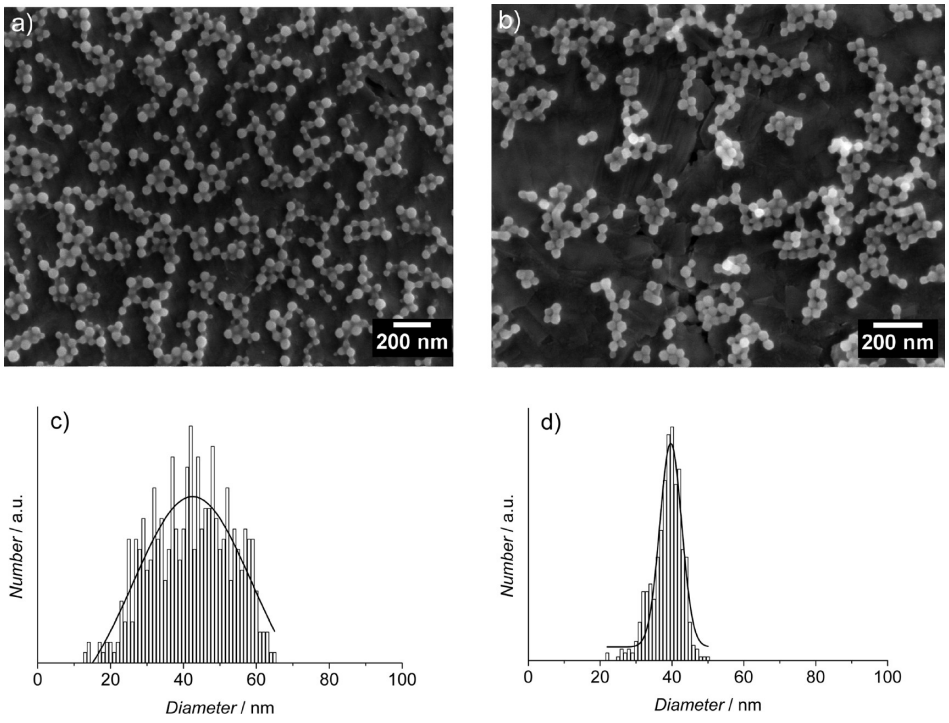


**Figure 8.** SEM images of intermediate particles during the formation of 65 nm-sized nanocrystals in the absence of a modulating ligand (a) after 240 s and (b) 1 h. Corresponding particle size distributions (c) after 240 s and (d) 1 h (the lines represent Gaussian fits).


dx.doi.org/10.1021/cm103571y |*Chem. Mater.* 2011, 23, 2130–2141

terminate at nearly the same size, before "defocusing" of size distribution takes place in later stages due to growth of larger particles at the expense of smaller ones (Ostwald ripening).[8,34] The observations clearly demonstrate that time is an important parameter to be considered when targeting monodisperse MOF nanocrystals.

**Time-Resolved in Situ SLS and ex Situ SEM Investigations of Microcrystal Formation.** SLS measurements were successfully performed with synthesis solutions of composition Zn/Hmim/L/MeOH = 1:4:4:1000 (L = formate and 1-methylimidazole), yielding microcrystals. The systems behave quite differently from those yielding nanocrystals. As can be seen from Figure 6b, in the case of microcrystal formation with formate as a modulating ligand, SLS enables the first significant size evaluation of particles ($R_g \approx 50$ nm) after approximately 350 s. The particle size rapidly increases with time, as does the total particle mass. Since the correlation of $R_g$ with time is almost linear between 350 and 480 s, an estimate for the starting point of particle formation after mixing (induction time, $t_{ind}$) has been obtained as the intercept of the backward extrapolated curve with the abscissa ($t_{ind} = 280$ s). At 480 s, when the particles have grown to $R_g \approx 110$ nm, an abrupt change is clearly seen in the correlation of $R_g$ with time, indicating a change in the mechanism of particle growth (see below). Beyond that point, growth in size and mass continues and could be safely monitored by SLS up to 950 s ($R_g \approx 220$ nm). Thereafter, sedimentation of larger particles was indicated by a beginning decrease of the scattering intensity.

Significant insight into the mechanism of particle growth can be obtained from the exponent α of the power law relation between $R_g$ and $M_W$, $R_g \sim M_W^{\alpha}$. On the log($R_g$) vs log($M_W$) plot displayed in Figure 7b, the slope before and after 480 s corresponds to α = 0.29 and α = 0.15, respectively. Interestingly, these values are close to the values predicted recently by some of us[29] for spherical particles that grow by coalescence (α = 1/3) or according to a monomer addition model (α = 1/6). The same exponents are expected for particles with a cubic symmetry. The SEM investigations presented below support the assumption that intermediate particles in the course of ZIF-8 growth are isometrical. Thus, we may infer from the SLS data that ZIF-8 microcrystals grow, under the conditions studied here, by two consecutive mechanisms: (i) particle aggregation comparable to coalescence and (ii) particle−monomer attachment.

A similar pattern of growth is observed in the case of microcrystal formation with 1-methylimidazole as a modulating ligand (see Figure 6c). The first significant particle size values ($R_g \approx 50$ nm) are detected by SLS after approximately 500 s ($t_{ind}$ = 350 s). The particles continuously grow in size and mass until 1200 s, corresponding to the last point shown in Figure 4c ($R_g \approx$ 180 nm). However, a careful inspection of the log($R_g$) vs log($M_W$) plot displayed in Figure 7c reveals a bent curve, which only enables the estimate of a final slope after 800 s corresponding to α = 0.19. Thus, we may infer form the SLS data that coalescence and monomer attachment simultaneously take place during early stages of growth, while monomer attachment dominates in later stages.

For larger particles ($R_g$ > 100 nm), information on their shape can be obtained from the SLS curves. Scattering patterns with the intensity $I(q)$ in its normalized form $P(q) = I(q)/I(q = 0)$ are displayed for selected intermediates of microcrystal formation in the presence of formate and 1-methylimidazole in Figure 9a,b, respectively. The data are compared with theoretically predicted

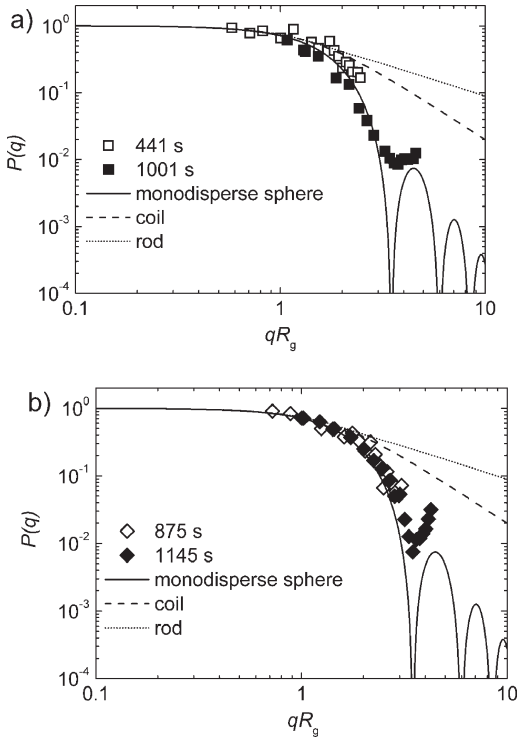


**Figure 9.** Normalized scattering intensity, $P(q)$, vs rescaled scattering vector modulus, $q \cdot R_g$, for two intermediates during the formation of microcrystals in the presence of (a) sodium formate and (b) 1-methylimidazole. Theoretical curves for monodisperse spheres, coils, and rods are shown for comparison.

curves for noninteracting particles of different morphologies, namely, monodisperse spheres,[35] coils,[36] and rods.[37] To better illustrate the shape selectivity, the scattering vector modulus $q$ has been rescaled to the size of the particles according to $u = q \cdot R_g$. In this dimensionless representation, curves from self-similar structures fall on top of each other, if the structures differ in size only. For both modulating ligands, the individual experimental curves overlay and are close to the curve predicted for monodisperse spheres, suggesting that the particles are compact and isometrical. The first oscillation which is clearly seen in the experimental curves is a strong indication of a narrow size distribution, since increasing polydispersity results in blurring of such oscillations.[13]

Complementary SEM and TEM investigations were carried out for the synthesis with 1-methylimidazole as a modulating ligand. We were able to observe particles that are clear intermediates in the course of ZIF-8 formation after approximately 600 s, which apparently belong to the particle−monomer growth process. The first particles seen on the SEM images have the shape of a cube ({100} crystal form) with rounded edges and a size of approximately 100 nm (see Figure 10a). After 2000 s, the particles still have the same shape but have grown to a size of 400 nm (see TEM image in Figure 10b), revealing that the relative growth rates of different faces are slowest along the ⟨100⟩ directions. The sharp spots seen on the ED pattern in Figure 10c, which is a view down a ⟨100⟩ zone axis with fourfold rotational symmetry, demonstrate that the cube-shaped particles are well crystalline ZIF-8. On the TEM image in Figure 10b, a thin rim around the nanocrystal with different electron density contrast is identified, which may, for example, indicate the presence of an


dx.doi.org/10.1021/cm103571y |Chem. Mater. 2011, 23, 2130–2141

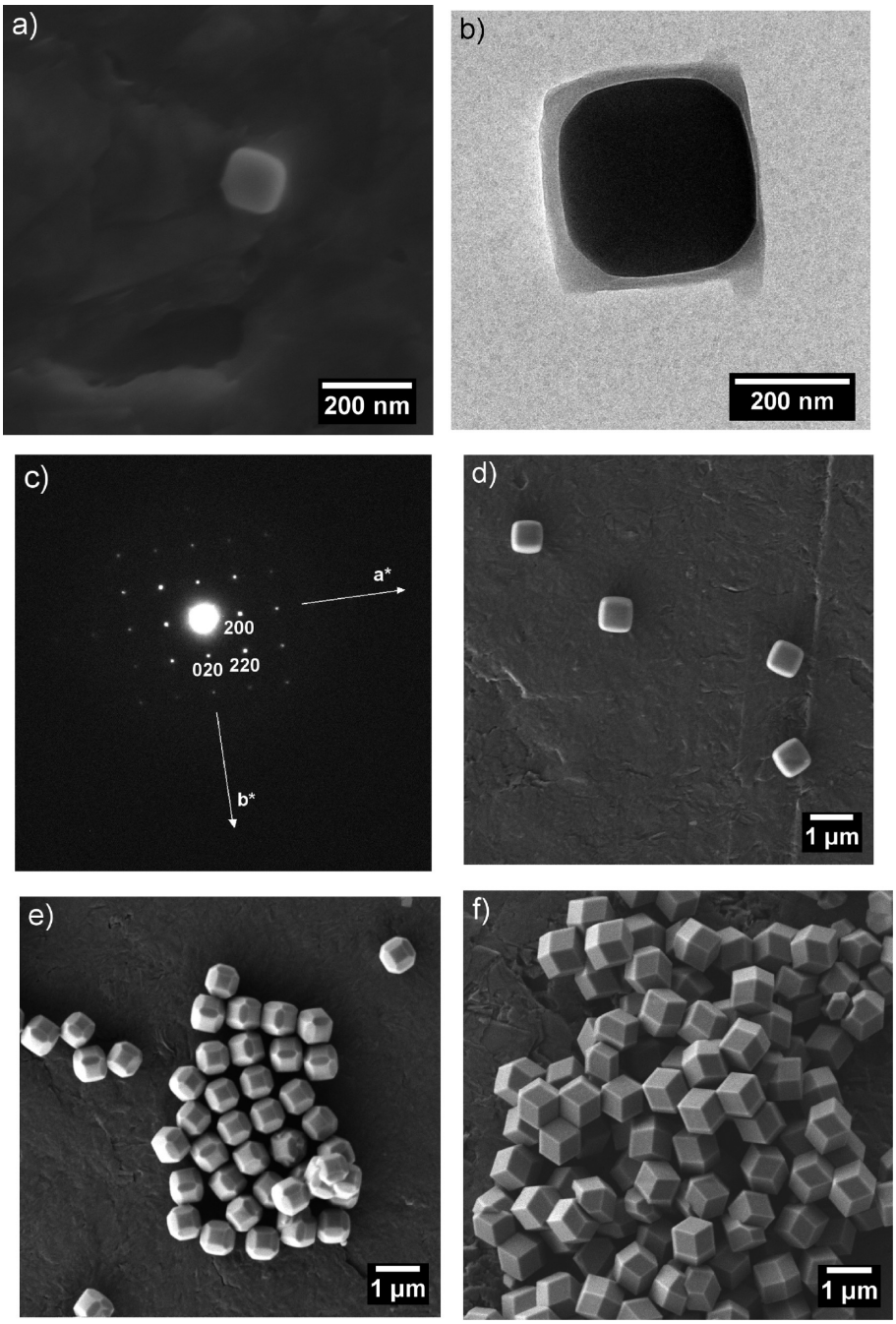


**Figure 10.** Intermediate particle during the formation of microcrystals in the presence of 1-methylimidazole: (a) SEM image of a particle after 600 s, (b) TEM image of a particle after 2000 s, (c) ED pattern of the particle after 2000 s, (d) SEM image of particles after 3000 s, (e) SEM image of particles after 5000 s, and (f) SEM image of particles after 24 h.

amorphous growth layer. The size distribution of the nanocrystals revealed by the SEM image taken after 3000 s (Figure 10d) appears to be rather narrow, in close agreement with the SLS data (oscillation in the scattering curve after 1145 s, Figure 9b). Beyond 4000 s, the nanocrystals change their shape due to a change in the relative growth rates, which are now slowest along ⟨110⟩ directions. On the SEM image taken after 5000 s, 500 nm-sized cubes with truncated edges that expose 6 {100} and 12 {110} faces are seen (Figure 10e). The micrometer-sized crystals recovered after 24 h have a rhombic dodecahedral shape with exposed {110} faces (see SEM image in Figure 10f).

The formation of microcrystals in the presence of formate follows the same pattern of shape evolution from cubes with truncated edges to final rhombic dodecahedra (see the SEM images provided in Figure S7 of the Supporting Information). It should be noted here that SEM and TEM investigations on formate-containing systems are hampered much more seriously by species other than real ZIF-8 intermediates (e.g., sodium formate that deposits upon evaporating the dispersions prior to the SEM/TEM investigations) as is the case with 1-methylimidazole-containing systems. Due to uncertainty in the identity of species observed on SEM images taken during early stages of


dx.doi.org/10.1021/cm103571y |*Chem. Mater.* 2011, 23, 2130–2141

ZIF-8 microcrystal formation (an example is provided in Figure S8 of the Supporting Information), we cannot up to now verify the coalescence mechanism suggested by our SLS data. Before unambiguous information can be obtained by SEM/TEM, specific procedures for separating impurities have to be developed first.

From a coordination chemistry point of view, 1-methylimidazole is expected to be a stronger coordinating ligand to Zn(II) than formate. In agreement with this, addition of 1-methylimidazole results in a lower nucleation rate, as judged from the longer induction time (350 vs 280 s), and a lower growth rate, as indicated by the slower increase of the $R_g$ and $M_W$ values with time. In addition, the change of shape from cubes to rhombic dodecahedra occurs at later times in the presence of 1-methylimidazole than of formate.

A comparison of the SLS data of the modulated and nonmodulated syntheses points to an interesting difference between both types of crystallization processes. During the first 800 s, the apparent weight-averaged particle mass $M_W$ recorded in the absence of a modulating ligand exeeds considerably the $M_W$ values measured in the presence of either modulating ligand. As can be seen from Figures 6 and 7, the difference amounts to more than a magnitude. This is particularly intriguing as the particle size values are much smaller if modulating ligands are absent. However, in order to better judge this feature, the physical meaning and origin of the apparent mass values have to be briefly outlined. The values are directly taken from the intercepts of the scattering curves (see Supporting Information) and thus are proportional to the solid mass concentration times the apparent weight averaged solid mass. Now, this product can be looked at from two different perspectives:[39] (i) since the solid concentration in $g \cdot L^{-1}$ is a constant determined by weight and is not changing during the growth process, the intercept can be considered to be directly proportional to the weight averaged mass including all species, that is, monomers and growing particles, and (ii) the monomers can to a good approximation be considered as species with a negligible scattering contribution, which means that the intercept increases via the concentration of the generated and growing particles and/or via the growing particle mass (now excluding the monomer fraction). If we adopt the latter perspective, the discrepancy in apparent mass values for the two growth processes is immediately understandable: In the absence of modulating ligands, the increase of weight-averaged apparent mass values is due to a persisting nucleation during at least the first 800 s. In the presence of either modulating ligand, we observe a simultaneous growth of both the averaged size and the apparent mass values. Despite the much larger size values achieved in this case, the respective mass values are considerably lower because the number of particles and with it the mass concentration of particles are much lower in the latter case. This is due to the fact that the extent of nucleation has to be much lower and perhaps even ceases entirely before 800 s if modulating ligands are present. Thus, the SLS data provide clear direct evidence from in situ experiments that a function of modulating ligands of comparatively low bacisity ($pK_a < 10.3$ in our case) is to slow down the nucleation rate, as proposed above and previously by Kitagawa and co-workers[12b] on the basis of systematic synthetic work.

**Investigation of Thermal Stability and Porosity.** All prepared ZIF-8 materials exhibit good thermal stability in air, up to 250 °C in the case of the smaller 18 nm-sized nanocrystals, and up to 300 °C in the case of the larger nanocrystals and microcrystals. This is demonstrated by TG/DTA curves (see Figure S9 of the Supporting Information) as well as variable-temperature XRD patterns (see Figure S10 of the Supporting Information). Since nearly no mass loss is seen on the TG curves before the onset of the exothermic decomposition of the organic bridging ligand, it is clear that solvent (MeOH) and modulator molecules have already left the intracrystallite cavities during workup (drying) after synthesis. Hence, no further solvent exchange and/or heat treatment procedures are necessary for activation of the materials.

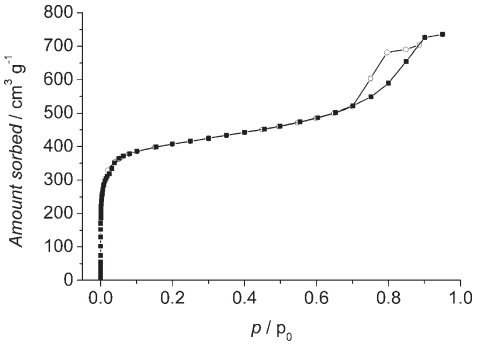


**Figure 11.** (a) Nitrogen sorption isotherms at −196 °C for the 18 nm-sized nanocrystals prepared in the presence of *n*-butylamine. Black squares: adsorption branch; open dots: desorption branch.

On the $N_2$ sorption isotherms of the 18 nm-sized nanocrystals (Figure 11), a first steep step at low relative pressure ($p/p_0 < 0.08$) is seen, revealing that the nanocrystals are microporous. The specific surface area estimated by the BET method amounts to $S_{BET} = 1617\ m^2 \cdot g^{-1}$. The value compares well with those reported recently for ZIF-8 macrocrystals ($S_{BET} = 1630\ m^2 \cdot g^{-1}$)[6a] and ~30 nm-sized ZIF-8 nanocrystals ($S_{BET} = 1696\ m^2 \cdot g^{-1}$).[21] This confirms that the 18 nm-sized nanocrystals are well crystalline, as already evidenced by XRD and SAED. The isotherms exhibit a second step at high relative pressure ($p/p_0 > 0.7$) with an adsorption−desorption hysteresis loop of type H2.[38] The step originates from interparticle mesopores, demonstrating the dual micro- and mesoporosity of the ZIF-8 nanocystal powders. The mesopore size distribution estimated by the BJH method is centered at ~8 nm. Small crystal size and dual porosity are of interest for the development of advanced adsorbents and catalysts with fast mass transport kinetics. Indeed, a significant increase of adsorption rates of nanocrystals compared to microcrystals was recently demonstrated for ZIF-8 (~45 nm-sized nanocrystals)[18] and the flexible MOF [Zn(ip)(bpy)] (CID-1, ip = isophthalate, byp = 4,4′-bipyridyl).[10f]

## CONCLUSION

We have reported a novel synthetic approach to ZIF-8 nano- and microscale materials in which size-control between ~10 nm and 1 $\mu$m is achieved by employing an excess of the bridging bidentate ligand and three simple auxiliary modulating ligands that act as competitive ligands in coordination equilibria and bases in deprotonation equilibria during nucleation and growth. Time-resolved in situ SLS and ex situ SEM/TEM investigations have provided insight into the functioning of modulating ligands. Furthermore, the experiments have revealed that nanocrystal formation is characterized by continuous, comparatively slow nucleation and fast crystal growth. A focusing of the nanocrystal size distribution occurs with increasing time, resulting in a very narrow size distribution at the size focusing point, and is followed

by defocusing of the size distribution at later stages of the growth. The growth of microcrystals takes place by a particle−monomer attachment mechanism, and a change of crystal shape from cubes to rhombic dodecahedra occurs in later stages of growth. Furthermore, indications for the occurrence of a coalescence mechanism during early stages of the growth have been obtained. The prepared ZIF-8 materials are easily activated (due to the use of MeOH as the solvent) and exhibit good thermal stability in air as well as large surface areas, which are comparable to those of large macrocrystals. Nanocrystal powders exhibit dual micro- and mesoporosity.

The novel synthetic strategy and insight into the crystallization processes may help to put size- and shape-controlled syntheses of nano- and microscale bulk ZIF materials and supported ZIF membranes and films on a more rational basis. Indeed, the recent successful synthesis of ZIF-7 nanocrystals by employing an excess of the bridging benzimidazolate ligand[4b] indicates that the synthetic principles reported here may be transferable to other ZIF and possibly even to other MOF systems.

While the manuscript was under reviewing two papers appeared in the literature which are related to the work presented herein: Pan et al.[40] report the rapid synthesis of ZIF-8 nanocrystals being between ~50 and 85 nm in size. Their protocols differ from ours in the use of water (instead of MeOH) as the solvent and a much larger excess of the bridging Hmim ligand (Hmim/Zn ≥ 70:1). Venna et al.[41] report an ex situ XRD and TEM study of the formation of ZIF-8 nanocrystals at room temperature in the presence of an excess of the bridging Hmim ligand (Hmim/Zn = 8:1). They concluded that the crystallization process is nucleation-controlled. This is in general agreement with our findings by in situ SLS and ex situ SEM.

## ■ ASSOCIATED CONTENT

**Supporting Information.** Details of syntheses, SLS measurements, comments on nanocrystal shape, SAXS/PDDF, SEM, XRD, TG/DTA, variable-temperature XRD, nitrogen physisorption, and FT-IR data (PDF).This material is available free of charge via the Internet at http://pubs.acs.org.

## ■ AUTHOR INFORMATION

### Corresponding Author

*E-mail: michael.wiebcke@acb.uni-hannover.de (M.W.), klaus.huber@chemie.uni-paderborn.de (K.H.).

## ■ ACKNOWLEDGMENT

The authors thank G. Platz for performing the physisorption measurements. The work was supported by the Deutsche Forschungsgemeinschaft (DFG) within the frame of the Priority Progam 1362 (Porous Metal−Organic Frameworks) organized by S. Kaskel. The authors gratefully acknowledge the funding by the DFG (Grants WI1156/2-1 and HU807/12-1).

## ■ REFERENCES

(1) Phan, A.; Doonan, C. J.; Uribe-Romo, F. J.; Knobler, C. B.; O'Keeffe, M.; Yaghi, O. M. *Acc. Chem. Res.* **2010**, *43*, 58.

(2) (a) Yaghi, O. M.; O'Keeffe, M.; Ockwig, N. W.; Chae, H. K.; Eddaoudi, M.; Kim, J. *Nature* **2003**, *423*, 705. (b) Kitagawa, S.; Kitaura, R.; Noro, S. *Angew. Chem., Int. Ed.* **2004**, *43*, 2334. (c) Férey, G. *Chem. Soc. Rev.* **2008**, *37*, 191.

(3) (a) Banerjee, R.; Phan, A.; Wang, B.; Knobler, C.; Furukawa, H.; O'Keeffe, M.; Yaghi, O. M. *Science* **2008**, *319*, 939. (b) Banerjee, R.; Furukawa, H.; Britt, D.; Knobler, C.; O'Keeffe, M.; Yaghi, O. M. *J. Am. Chem. Soc.* **2009**, *131*, 3875. (c) Li, K.; Olson, D. H.; Seidel, J.; Emge, T. J.; Gong, H.; Zeng, H.; Li, J. *J. Am. Chem. Soc.* **2009**, *131*, 10368. (d) Morris, W.; Leung, B.; Furukawa, H.; Yaghi, O. K.; He, N.; Hayashi, H.; Houndonougbo, Y.; Asta, M.; Laird, B. B.; Yaghi, O. M. *J. Am. Chem. Soc.* **2010**, *132*, 11006. (e) Chizallet, C.; Lazare, S.; Bazar-Bachi, D.; Bonnier, F.; Lecocq, V.; Soyer, E.; Quoineaud, A.-A.; Bats, N. *J. Am. Chem. Soc.* **2010**, *132*, 12365.

(4) (a) Bux, H.; Liang, F.; Li, Y.; Cravillon, J.; Wiebcke, M.; Caro, J. *J. Am. Chem. Soc.* **2009**, *131*, 16000. (b) Li, Y.; Liang, F.; Bux, H.; Feldhoff, A.; Yang, W.-S.; Caro, J. *Angew. Chem., Int. Ed.* **2010**, *49*, 548. (c) McCarthy, M. C.; Varela-Guerrero, V.; Barnett, G. V.; Jeong, H.-K. *Langmuir* **2010**, *26*, 14636. (d) Huang, A.; Bux, H.; Steinbach, F.; Caro, J. *Angew. Chem., Int. Ed.* **2010**, *49*, 4958. (e) Lu, G.; Hupp, J. T. *J. Am. Chem. Soc.* **2010**, *132*, 7832. (f) Aguado, S.; Canivet, J.; Farrusseng, D. *Chem. Commun.* **2010**, *46*, 7999.

(5) (a) Tian, Y.-Q.; Cai, C.-X.; Ji, Y.; You, X.-Z.; Peng, S.-M.; Lee, G.-H. *Angew. Chem., Int. Ed.* **2002**, *41*, 1384. (b) Wu, T.; Zhang, J.; Zhou, C.; Wang, L.; Bu, X.; Feng, P. *J. Am. Chem. Soc.* **2009**, *131*, 6111. (c) Tian, Y.-Q.; Yao, S.-Y.; Gu, D.; Cui, K.-H.; Guo, D.-W.; Zhang, G.; Chen, Z.-X.; Zhao, D.-Y. *Chem.—Eur. J.* **2010**, *16*, 1137.

(6) (a) Park, K. S.; Ni, Z.; Côté, A. P.; Choi, J. Y.; Huang, R.; Uribe-Romo, F. J.; Chae, H. K.; O'Keeffe, M.; Yaghi, O. M. *Proc. Natl. Acad. Sci. U.S.A.* **2006**, *103*, 10186. (b) Huang, X.-C.; Lin, Y.-Y.; Zhang, J.-P.; Chen, X.-M. *Angew. Chem., Int. Ed.* **2006**, *45*, 1557.

(7) Tosheva, L.; Valtshev, V. P. *Chem. Mater.* **2005**, *17*, 2494.

(8) Park, J.; Joo, J.; Kwon, S. G.; Jang, Y.; Hyeon, T. *Angew. Chem., Int. Ed.* **2007**, *46*, 4630.

(9) (a) Spokoyny, A. M.; Kim, D.; Sumrein, A.; Mirkin, C. A. *Chem. Soc. Rev.* **2009**, *38*, 1218. (b) Lin, W.; Rieter, W. J.; Taylor, K. M. L. *Angew. Chem., Int. Ed.* **2009**, *48*, 650. (c) McKinlay, A. C.; Morris, R. E.; Horcajada, P.; Férey, G.; Gref, R.; Couvreur, P.; Serre, C. *Angew. Chem., Int. Ed.* **2010**, *49*, 6260.

(10) (a) Huang, L.; Wang, H.; Chen, J.; Wang, Z.; Sun, J.; Zhao, D.; Yan, Y. *Microporous Mesoporous Mater.* **2003**, *58*, 105. (b) Qiu, L.-G.; Li, Z.-Q.; Wu, Y.; Wang, W.; Xu, T.; Jiang, X. *Chem. Commun.* **2008**, 3642. (c) Taylor-Pashow, K. M. L.; Rocca, J. D.; Xie, Z.; Tran, S.; Lin, W. *J. Am. Chem. Soc.* **2009**, *131*, 14261. (d) Horcajada, P.; Chalati, T.; Serre, C.; Gillet, B.; Sebrie, C.; Baati, T.; Eubank, J. F.; Heurtaux, D.; Clayette, P.; Kreuz, C.; Chang, J.-S.; Hwang, Y. K.; Marsaud, V.; Bories, P.-N.; Cynober, L.; Gil, S.; Férey, G.; Couvreur, P.; Gref, R. *Nat. Mater.* **2010**, *9*, 172. (e) Guillerm, V.; Gross, S.; Serre, C.; Devic, T.; Bauer, M.; Férey, G. *Chem. Commun.* **2010**, *46*, 767. (f) Tanaka, D.; Henke, A.; Albrecht, K.; Moeller, M.; Nakagawa, K.; Kitagawa, S.; Groll, J. *Nat. Chem.* **2010**, *2*, 410.

(11) (a) Hermes, S.; Witte, T.; Hikov, T.; Zacher, D.; Bahnmüller, S.; Langstein, G.; Huber, K.; Fischer, R. A. *J. Am. Chem. Soc.* **2007**, *129*, 5324. (b) Horcajada, P.; Serre, C.; Grosso, D.; Boissière, C.; Perruchas, S.; Sanchez, C.; Férey, G. *Adv. Mater.* **2009**, *21*, 1931.

(12) (a) Tsuruoka, T.; Furukawa, S.; Takashima, Y.; Yoshida, K.; Isoda, S.; Kitagawa, S. *Angew. Chem., Int. Ed.* **2009**, *48*, 4739. (b) Diring, S.; Furukawa, S.; Takashima, Y.; Tsuruoka, T.; Kitagawa, S. *Chem. Mater.* **2010**, *22*, 4531.

(13) Zacher, D.; Lin, J.; Huber, K.; Fischer, R. A. *Chem. Commun.* **2009**, 1031.

(14) Shekhah, O.; Wang, H.; Zacher, D.; Fischer, R. A.; Wöll, C. *Angew. Chem., Int. Ed.* **2009**, *48*, 5038.

(15) John, N. S.; Scherb, C.; Shöâeè, M.; Anderson, M. W.; Attfield, M. P.; Bein, T. *Chem. Commun.* **2009**, 6294.

(16) Millange, F.; Medina, M. I.; Guillou, N.; Férey, G.; Golden, K. M.; Walton, R. I. *Angew. Chem., Int. Ed.* **2010**, *49*, 763.

(17) Cravillon, J.; Münzer, S.; Lohmeier, S.-J.; Feldhoff, A.; Huber, K.; Wiebcke, M. *Chem. Mater.* **2009**, *21*, 1410.

(18) Ostermann, R.; Cravillon, J.; Weidmann, C.; Wiebcke, M.; Smarsly, B. M. *Chem. Commun.* **2010**, *47*, 442.
(19) Venna, S. R.; Carreon, M. A. *J. Am. Chem. Soc.* **2010**, *132*, 76.
(20) Bux, H.; Feldhoff, A.; Cravillon, J.; Wiebcke, M.; Li, Y.; Caro, J. *Chem. Mater.* **2011**, accepted.
(21) Demessence, A.; Boissière, C.; Grosso, D.; Horcajada, P.; Serre, C.; Férey, G.; Soler-Illia, G. J. A. A.; Sanchez, C. *J. Mater. Chem.* **2010**, *20*, 7676.
(22) Chang, N.; Gu, Z.-Y.; Yan, X.-P. *J. Am. Chem. Soc.* **2010**, *132*, 13645.
(23) Nune, S. K.; Thallapally, P. K.; Dobnalkova, A.; Wang, C.; Liu, J.; Exarbos, G. J. *Chem. Commun.* **2010**, *46*, 4878.
(24) Li, Y.; Bux, H.; Feldhoff, A.; Li, G.-L.; Yang, W.-S.; Caro, J. *Adv. Mater.* **2010**, *22*, 3322.
(25) Kline, S. R. *J. Appl. Crystallogr.* **2006**, *39*, 895.
(26) Glatter, O.; Kratky, O. *Small Angle X-ray Scattering*; Academic Press: London, 1982.
(27) Konarev, P. V.; Petoukhov, M. V.; Volkov, V. V.; Svergun, D. I. *J. Appl. Crystallogr.* **2006**, *39*, 277.
(28) Becker, A.; Schmidt, M. *Macromol. Chem. Macromol. Symp.* **1991**, *50*, 249.
(29) Liu, J.; Rieger, J.; Huber, K. *Langmuir* **2008**, *24*, 8262.
(30) Guinier, A.; Fournet, G. *Small-Angle Scattering of X-Rays*; Wiley: New York, 1955.
(31) Mullin, J. W. *Crystallization*, 4th ed.; Butterworth-Heinemann: Oxford, 2001.
(32) Rath, T.; Kunert, B.; Resel, R.; Fritz-Popovski, G.; Saf, R.; Trimmel, G. *Inorg. Chem.* **2008**, *47*, 3014.
(33) Kimura, E.; Kurogi, Y.; Shionoya, M.; Shiro, M. *Inorg. Chem.* **1991**, *30*, 4524.
(34) Peng, X.; Wickham, J.; Alivisatos, A. P. *J. Am. Chem. Soc.* **1998**, *120*, 5343.
(35) Rayleigh, L. *Proc. R. Soc. London, Ser. A* **1914**, *90*, 219.
(36) Debye, P. *J. Phys. Colloid Chem.* **1947**, *51*, 18.
(37) Neugebauer, T. *Ann. Phys.* **1943**, *434*, 509.
(38) Sing, K. S. W.; Everett, D. H.; Haul, R. A. W.; Moscou, L.; Pierotti, R. A.; Rouquérol, J.; Siemieniewska, T. *Pure Appl. Chem.* **1985**, *57*, 603.
(39) Liu, J.; Pancera, S.; Boyko, V.; Shukla, A.; Narayanan, T.; Huber, K. *Langmuir* **2010**, *26*, 17405.
(40) Pan, Y.; Liu, Y.; Zeng, G.; Zhao, L.; Lai, Z. *Chem. Commun.* **2011**, *47*, 2071.
(41) Venna, S. R.; Jasinski, J. B.; Carreon, M. A. *J. Am. Chem. Soc.* **2010**, *132*, 18030.